



Article

Enhanced Methylene Blue Adsorption by Cu-BTC Metal-Organic Frameworks with Engineered Particle Size Using Surfactant Modulators

Shanli Wang¹, Lu Zhang¹, Mingyan Zhang¹, Licong Xu¹, Qian Hu¹, Tao Yang² , Kaili Tu¹, Minghua Wu¹ and Deyou Yu^{1,3,4,*} 

- ¹ Engineering Research Center for Eco-Dyeing and Finishing of Textiles (Ministry of Education), College of Textile Science and Engineering, Zhejiang Sci-Tech University, Hangzhou 310018, China; wsl33125@163.com (S.W.); ZhangLu_137997@163.com (L.Z.); 2020327130033@mails.zstu.edu.cn (M.Z.); xlc15838352137@163.com (L.X.); huqian163youxiang@163.com (Q.H.); 18257344700@163.com (K.T.); wmh@zstu.edu.cn (M.W.)
- ² Institute for Nanomaterials, Advanced Technologies and Innovation, Technical University of Liberec, 46117 Liberec, Czech Republic; tao.yang@tul.cz
- ³ Tongxiang Research Institute, Zhejiang Sci-Tech University, Tongxiang 345000, China
- ⁴ Xiangshan Knitting Institute, Zhejiang Sci-Tech University, Ningbo 315700, China
- * Correspondence: yudeyou92@zstu.edu.cn

Abstract: Metal-organic frameworks (MOFs) featuring porous structures and large specific surface areas have shown great potential in removing organic pollutants from wastewater via adsorption processes. Although the particle size of MOFs determines the adsorption performance (something known as the size-dependent effect), engineering it into desirable dimensions for enhancing the adsorption performance is a great challenge. Here, we develop a practical and facile approach to regulate the particle size of copper benzene-1,3,5-tricarboxylate (Cu-BTC) adsorbents with high tunability by screening the functional modulator of various surfactants adding in hydrothermal synthesis procedure. The effect of surfactant type and concentration on the particle size of Cu-BTC was systematically investigated. The results show that the nonionic surfactant polyvinylpyrrolidone (PVP) demonstrated the greatest ability to control the particle size of Cu-BTC among other counterparts (e.g., N, N, N-trimethyl-1-dodecanaminium bromide (DTAB), polyethylene glycol (PEG1000), sodium dodecyl sulfate (SDS), sodium dodecyl benzene sulfonate (SDBS) and hexadecyl trimethyl ammonium bromide (CTAB)). By increasing the PVP concentration to 0.14 mmol L⁻¹, the average particle size of Cu-BTC could be correspondingly reduced by more than ten times, reaching to a comparative smaller value of 2.4 μm as compared with the reported counterparts. In addition, the PVP allowed a large increase of the surface area of Cu-BTC according to porosity analysis, resulting in a great enhancement of methylene blue (MB) adsorption. The PVP-modulated Cu-BTC showed fast adsorption kinetics for MB removal accompanied with a maximum adsorption capacity of 169.2 mg g⁻¹, which was considerably competitive with most of the analogs reported. Therefore, our study may inspire concepts for engineering the particle size of Cu-BTCs with improved properties for more practical applications.

Keywords: Cu-BTC; particle size; adsorption; surfactant; modulator



Citation: Wang, S.; Zhang, L.; Zhang, M.; Xu, L.; Hu, Q.; Yang, T.; Tu, K.; Wu, M.; Yu, D. Enhanced Methylene Blue Adsorption by Cu-BTC Metal-Organic Frameworks with Engineered Particle Size Using Surfactant Modulators. *Water* **2022**, *14*, 1864. <https://doi.org/10.3390/w14121864>

Academic Editor: Tushar Kanti Sen

Received: 6 May 2022

Accepted: 8 June 2022

Published: 10 June 2022

Publisher's Note: MDPI stays neutral with regard to jurisdictional claims in published maps and institutional affiliations.



Copyright: © 2022 by the authors. Licensee MDPI, Basel, Switzerland. This article is an open access article distributed under the terms and conditions of the Creative Commons Attribution (CC BY) license (<https://creativecommons.org/licenses/by/4.0/>).

1. Introduction

The continuous growth of the textile industry produces a lot of wastewater commonly discharged from dyeing and printing processes. Toxic and refractory components, such as dyes, auxiliaries, and by-products in the textile wastewater pose significant risks to human health and the environment unless suitable treatments are implemented. In particular, methylene blue (MB), one of the most typical dyes, not only deteriorates water quality, but also has a significant impact on human health due to its toxic, carcinogenic, mutagenic

or teratogenic effects [1]. Recently, adsorption [2], membrane separation [3], advanced oxidation [4], and electrochemical process [5,6] have been well-developed and improved to purify dye pollutants. In particular, adsorption is widely used for wastewater treatment because of its low-cost, easy operation and mature facility [7–9]. However, one of the key components—adsorbent material, such as activated carbon [1], zeolite [10], and cellulose derivative [11]—that determines the overall treatment efficiency commonly fails to extract aqueous pollutants in an effective way and thus requires further improvement to largely optimize the balance between operating costs and performance [12]. To this end, developing advanced functional adsorbents with high adsorption performance is highly desired.

Metal–organic frameworks (MOFs) are a new type of inorganic–organic hybrid three-dimensional porous material constructed by metal ions/clusters and organic ligands. Most MOFs have been attracting extensive attention in adsorption usage due to their highly specific surface area, rich pore structure and adjustable physicochemical structure. Among the often reported MOFs, copper benzene-1,3,5-tricarboxylate (Cu-BTC) is a very representative compound for versatile applications, including high-efficiency adsorptive removal of aqueous pollutants, due to its easy preparation and low cost [1,13–16]. Specifically, Cu-BTC has a unique double connected network with main and secondary channel diameters of 0.9 and 0.5 nm [17–19], respectively. The cavity formed along the channel connection may function as useful space for the capture and storage of guests (e.g., dyes, metals and gas). Note that the structure part of Cu-BTC serving as active sites for adsorbing distinct guests is usually different and recognized in a different mechanistic manner.

There are many approaches developed for Cu-BTC preparation, such as hydrothermal synthesis [20], ultrasonic [21], microwave [22], freeze-drying [23] and electrochemical methods [24]. Among these, hydrothermal synthesis is one of the most widely used methods because of its simple reaction condition, high yield and good crystalline properties. Typically, Cu-BTC crystalline particles prepared by hydrothermal method are often not smaller than 20 μm [25,26], resulting in a relative lower accessible surface area and probably poor adsorption capacity toward organic dyes. However, scarce studies have been focused on the regulation of Cu-BTC's particle size during hydrothermal synthesis, which majorly controls accessible surface area and thus governs the adsorption performance via optimization of the mass transfer kinetics. In the case of targeting larger guest molecules than the porous diameter of Cu-BTC, the outer surface is more conducive to accommodate the pollutants because of the mismatching size effect. Consequently, well-shaped Cu-BTC featuring a smaller particle size is expected to enhance the adsorption performance for organic dye removal as more outer surface is potentially exposed to the guest molecules for attachment [27,28]. Unfortunately, little is known and reported about facile and practical methods on engineering the particle size of Cu-BTC for dye adsorption enhancement.

This study was inspired by the modulation function of surfactants on the size regulation of metal oxides crystals [29,30]. Up to now, the main strategy of morphology control was based on a coordination modulation regime, in which different additives such as surfactants are used to adjust crystal growth by influencing coordination balance [31]. Pan et al., proved that the existence of cationic surfactant switched the morphology of ZIF-8 MOFs, from truncated cube to rhombic dodecahedron [32]. Herein, we have, for the first time, evaluated the modulation efficiency of various anionic, cationic and nonionic surfactants featuring molecular structure diversities for engineering Cu-BTC's particle size by adding them into hydrothermal precursor solutions. The differences of chemical structure between surfactant-modulated Cu-BTC and the pristine analog were elucidated by the X-ray diffraction (XRD), scanning electron microscope (SEM), X-ray photoelectron spectroscopy (XPS), Fourier transform infrared spectroscopy (FTIR) and Brunauer–Emmett–Teller (BET). As a concept of proof, the dye adsorption performance of Cu-BTC with optimized size enabled by the screened surfactant was systematically investigated and discussed in terms of kinetics and stability. Our work may provide a facile and practical approach for the modulation of Cu-BTC with a highly improved adsorption capacity toward organic pollutants.

2. Experimental and Characterization

2.1. Materials

Copper nitrate trihydrate ($\text{Cu}(\text{NO}_3)_2 \cdot 3\text{H}_2\text{O}$, 99%), 1,3,5-benzenetricarboxylic acid (H_3BTC , 98%), dodecyl trimethyl ammonium bromide (DTAB, 99%), polyethylene glycol-1000 (PEG1000, AR) and polyvinylpyrrolidone (PVP, AR) were all purchased from Aladdin Industrial Co., Ltd., Shanghai, China. Ethanol was obtained from Hangzhou Gaojing Fine Chemical Co. Ltd., Hangzhou, China. Sodium dodecyl sulfate (SDS, AR) and sodium dodecyl benzene sulfonate (SDBS, AR) were received from Comio chemical reagents Co., Ltd., China. Hexadecyl trimethyl ammonium bromide (CTAB, AR) was supported by Tianjin Dongli Tianda Chemical Reagents Factory, Tianjin, China. Methylene blue (MB, 82%) was obtained from Shanghai Zhanyun Chemical Co., Ltd., Shanghai, China. The reagents were used as received without further purification. Deionized water was used for all the experiments if necessary.

2.2. Preparation of Surfactant-Modulated Cu-BTC and Pristine Cu-BTC

Firstly, 0.831 g (ca. 3.4 mmol) of $\text{Cu}(\text{NO}_3)_2 \cdot 3\text{H}_2\text{O}$ and 0.399 g (1.8 mmol) of trimesic acid were dissolved in 18 mL deionized water and 18 mL of ethanol to form solution A and B, respectively. The concentration range was set according to the critical micelle concentration (CMC) of surfactants. The solution A and B were mixed before adding a certain amount of surfactant (e.g., DTAB, PEG1000, SDS, SDBS, CTAB and PVP). After stirring for 30 min, the resulting solution was transferred into an autoclave and maintained at 393 K for 12 h to complete the hydrothermal reaction. A blue precipitate was obtained and subjected to a thorough and successive centrifugation and by washing with a mixture of ethanol and deionized water ($v:v = 1:1$) three times. Finally, the surfactant-modulated Cu-BTC was obtained after drying the precipitate in the vacuum at a temperature of 333 K for 12 h. The resultant surfactant-modulated Cu-BTCs were referred as D-Cu-BTC, P-Cu-BTC, S1-Cu-BTC, S2-Cu-BTC, C-Cu-BTC, and PV-Cu-BTC when using DTAB, PEG1000, SDS, SDBS, CTAB and PVP as the modulator, respectively. By comparison, the pristine Cu-BTC was fabricated using the identical processes above excluding surfactant addition.

2.3. Characterization

The morphology and particle size of the prepared samples were evaluated by scanning electron microscopy (SEM, Phenom Pro, Shanghai, China). The particle size distribution of Cu-BTC particles was measured by Mastersizer 2000 particle size analyzer (Malvern, UK), and the particle size was analyzed by the spatial distribution (scattering spectrum) of the scattered light of the particle. The crystal structure of the prepared samples were analyzed by X-ray diffraction (XRD, Thermo ARL X'TRA, Waltham, MA, USA). Fourier transform infrared spectroscopy (FT-IR, Vertex70 Bruker, Karlsruhe, Germany) was employed to unravel the chemical structure and functional groups of surfactant-modulated Cu-BTC. A Thermo K-Alpha X-ray photoelectron spectroscopy (XPS) was applied to investigate the chemical composition and electronic structure of samples using $\text{Al-K}\alpha$ ($h\nu = 1486.71$ eV) as a radiation source. As for N_2 adsorption–desorption measurement, the samples were first out-gassed at 393 K for more than 12 h prior to the measurement. Specific surface area and total pore volume were calculated by the Brunauer–Emmett–Teller (BET) method. The pore size distribution was extracted from the desorption curve using the Barrett–Joyner–Halenda (BJH) method. The zeta-potentials (pH_z) of the Cu-BTC suspension with different pH values were analyzed using Malvern Nano-ZS90 NanoSizer.

2.4. Adsorption Experiments

For MB adsorption tests, 50 mg of adsorbent was immersed into 50 mL of 20 mg L^{-1} dye solution. The initial pH of MB solution was adjusted by 0.1 mol L^{-1} HCl and 0.1 mol L^{-1} NaOH. The conical flask was placed in a digital thermostatic oscillator under a stirring rate of 200 rpm for 4 h to complete the adsorption process. Subsequently, the filtrate was collected for further analysis after separation through a filter with a pore size

of 0.22 μm . All experiments were performed in triplicate, and the average values were determined and shown in the figures or tables. The concentration of MB in the adsorption suspension was evaluated by measuring the absorbance at a wavelength of 665 nm. The corresponding removal rate and adsorption capacity of MB were calculated according to Equations (1) and (2), respectively.

$$R = \frac{(C_0 - C_e)}{C_0} \times 100 \quad (1)$$

$$q_e = \frac{(C_0 - C_e) \times V}{m} \quad (2)$$

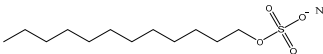
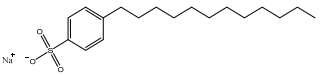
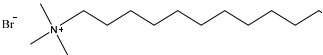
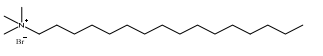
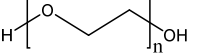
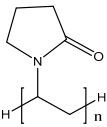
where C_0 (mg L^{-1}) and C_e (mg L^{-1}) are the initial and final concentration of the solution, V (L) is the volume of MB solution, and m (g) is the mass of adsorbent. To investigate the adsorption kinetics, water samples were taken from the adsorption stock at constant time intervals during 0 to 720 min for analysis. The adsorption isotherm experiments were performed using seven different initial MB concentrations ($10\text{--}800 \text{ mg L}^{-1}$). The effect of pH values on the adsorption of MB by Cu-BTC was also evaluated at pH values of 4.0, 5.0, 6.0, 7.0, 8.0, 9.0, 10.0, and 11.0.

3. Results and Discussion

3.1. Modulation Ability of Surfactants on the Particle Size of Cu-BTC

It was preliminarily observed that the surfactant is capable of reducing MOFs' particle size as it can mediate the crystal growth of MOFs in previously reports. Unfortunately, the modulation ability of surfactants with diverse structures is still unknown. As a concept of proof, we first investigated the efficiency of anionic, cationic and nonionic surfactants in modulating the particle size of Cu-BTC. To this end, two anionic surfactants (i.e., SDS and SDBS), cationic surfactants (i.e., DTAB and CTAB), and nonionic surfactants (i.e., PEG1000 and PVP) were selected for Cu-BTC preparations due to their totally different structures and commercial accessibility in Table 1. The effect of surfactants on the particle size of Cu-BTC are illustrated in Figure 1.

Table 1. Chemical structure and normalized cost of different surfactants.

Surfactant	Formula	Molecular Weight	Structural Diagram	* Cost (RMB ton^{-1} $\Delta\text{Particle Size}^{-1}$)
SDS	$\text{C}_{12}\text{H}_{25}\text{SO}_4\text{Na}$	288.38		4.4
SDBS	$\text{C}_{18}\text{H}_{29}\text{NaO}_3\text{S}$	348.476		0.9
DTAB	$\text{C}_{15}\text{H}_{34}\text{NBr}$	308.34		7
CTAB	$\text{C}_{19}\text{H}_{42}\text{BrN}$	364.46		2.8
PEG-1000	$\text{H}(\text{OCH}_2\text{CH}_2)_n\text{OH}$	1000		3.9
PVP	$(\text{C}_6\text{H}_9\text{NO})_n$	10,000		0.2

* Cost refers to particle size reduction normalized cost at the maximum efficiency.

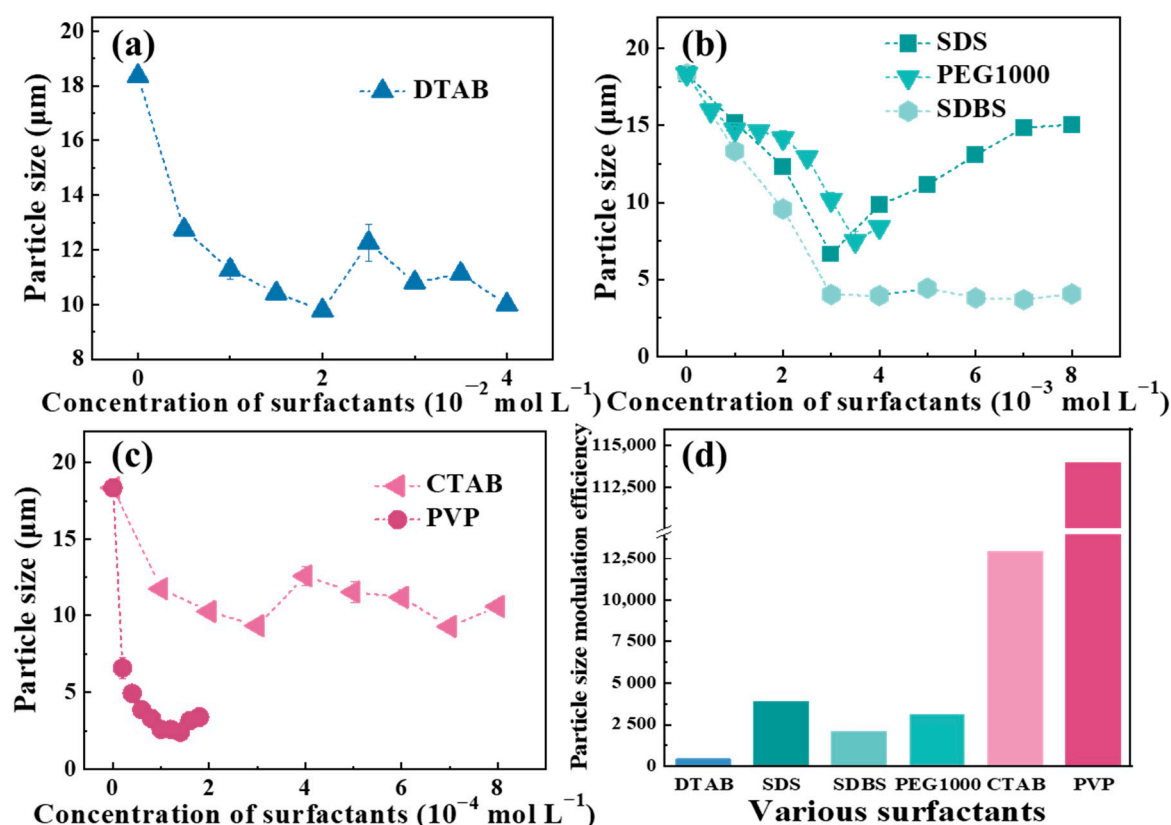


Figure 1. Effect of surfactants on the particle size of Cu-BTC: (a) DTAB; (b) SDS, SDBS, and PEG-100; (c) CTAB and PVP. (d) Concentration normalized particle size reduction of Cu-BTC using involved surfactants. Note that particle size modulation efficiency refers to the concentration normalized particle size reduction.

It can be seen from Figure 1a that the particle size of D-Cu-BTC is largely decreased from 18.4 to 9.8 μm as DTAB concentration increases from 0 to 20 mmol L⁻¹. When further increasing the concentration to 40 mmol L⁻¹, the particle size of D-Cu-BTC is found to be relatively steady rather than obviously decreasing. As for the effect of CTAB, it follows the same variation trend of particle size as DTAB, accompanied with a minimum C-Cu-BTC size of ca. 9.3 μm after adding more than 0.3 mmol L⁻¹ of CTAB in the hydrothermal synthesis formula. Remarkably, an inverted volcanic curve is observed for anionic surfactant SDS, whose function of modulation maximizes at the concentration of 3.0 mmol L⁻¹ with a resulting particle size of 6.6 μm. Meanwhile, another anionic surfactant SDBS exhibits an efficient performance in decreasing Cu-BTC's particle size (from 18.4 to 3.7 μm) over concentration ranges of 0–3.0 mmol L⁻¹. Similar changes in particle size of P-Cu-BTC are detected with the increasing addition of PEG1000. Although PEG1000 only reduces the particle size of Cu-BTC to 7.5 μm, the same analog surfactant PVP outperforms all the others in terms of the ability to reduce the particle size to a smallest level (ca. 2.4 μm). In addition, the concentration normalized particle size reduction of Cu-BTC using these surfactants (Figure 1d) suggests that the PVP also gives the highest modulation efficiency by using comparatively low concentrations among other five candidates. For instance, to fabricate the surfactant modulated Cu-BTC with a particle size of ca. 7.0 μm, about 3.0 mmol L⁻¹ of SDS, 3.5 mmol L⁻¹ of PEG1000, 2.5 mmol L⁻¹ of SDBS or only 0.2 mmol L⁻¹ of PVP addition is sufficient for preparation while the remaining candidates are totally invalid for reducing size to a value as small as ca. 7.0 μm.

In short, the PVP is found to have the best ability to modulate the particle size of Cu-BTC among applied surfactants. In particular, the poorest modulation ability of cationic surfactants DTAB and CTAB on the particle size of Cu-BTC could be ascribed into their

relatively lower dispersity in the aqueous solution. On the other hand, in the case of the same type of surfactant, it can be found that the surfactant having relatively bigger molecular weight (e.g., SDBS, PVP) is more reactive than those with smaller molecular weight (e.g., SDS, PEG1000) in controlling the particle size of Cu-BTC. This may be because the larger molecular weight along with longer molecular chain allows for the effective retardation of the growth of crystals via the space hindrance effect. In addition, as a polymeric surfactant and dispersant, PVP also contains a large amount of nitrogen atoms, whose lone pair electrons are expected to interact with copper atoms terminated in the crystals. By screening the types of surfactants as well as their usages, we could easily tailor the particle size of Cu-BTC from 18.4 to 2.4 μm with the addition of 0.02 to 0.14 mmol L^{-1} PVP. Finally, the P-Cu-BTC with a particle size of 2.4 μm was selected in particular to investigate the structural difference and dye adsorption enhancement below.

3.2. Structural Analysis of Surfactant Modulated and Pristine Cu-BTC

Figure 2 shows the SEM images of pristine Cu-BTC and PV-Cu-BTC. It can be clearly seen that both PV-Cu-BTC and pristine Cu-BTC demonstrate a regular octahedron, which matches well with previous reports [33,34]. However, an average particle size of ca. 2.4 μm is observed in PV-Cu-BTC's SEM image while pristine Cu-BTC is highlighted with a much larger dimension (ca. 20 μm). This indicates that PVP is practical and useful to mediate the crystal growth stage rather than nucleation process for smaller Cu-BTC particle preparation. In the hydrothermal system of crystallization, growing facets of Cu-BTC particles formed in the solution would be blocked by the fast interaction with both the hydrophobic long-chain alkyl group and the hydrophilic N moieties within PVP macromolecules. Once the PVP macromolecule is adsorbed onto the specific facet, it undergoes self-entanglement to create a steric hindrance effect, which may determine its capability to reduce the growth rate of Cu-BTC crystals and terminate them with similar shape but much smaller particle size.

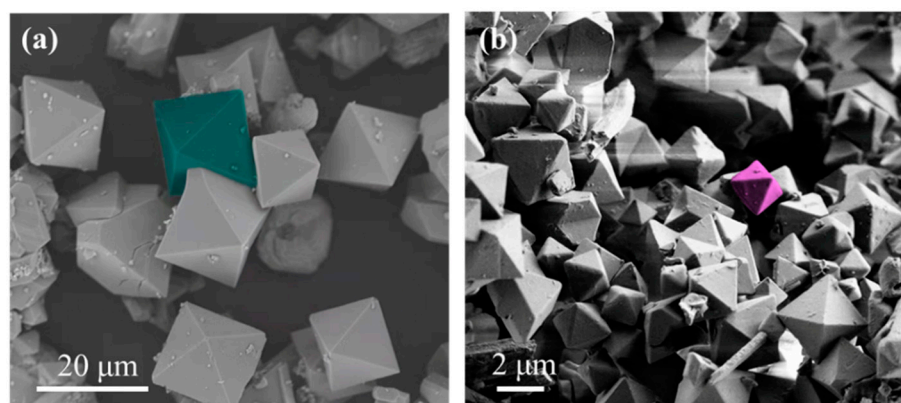


Figure 2. SEM images of pristine Cu-BTC (a) and PV-Cu-BTC (b).

To further investigate the influence of PVP on the molecular structure of Cu-BTC, the FT-IR spectra of PV-Cu-BTC and pristine Cu-BTC were recorded, as shown in Figure 3. The detected peak at 3419 cm^{-1} could be assigned to the hydroxyl (H-O) stretching vibration in carboxyl (-COOH), which is the functional organic linker to construct the sketch of Cu-BTC. The characteristic peaks belonging to the asymmetric and symmetric stretching vibration peaks of carboxyl were also observed at 1641 and 1444 cm^{-1} , respectively. In addition, the peak at 1373 cm^{-1} was assigned to the C-O bond stretching vibration while the peak at 730 cm^{-1} was the fingerprint band of the C-H in benzene rings. Comparing with the FT-IR spectrum of pristine Cu-BTC, little difference could be found in the case of PV-Cu-BTC, suggesting almost no chemical structural changes of Cu-BTC with PVP modulation.

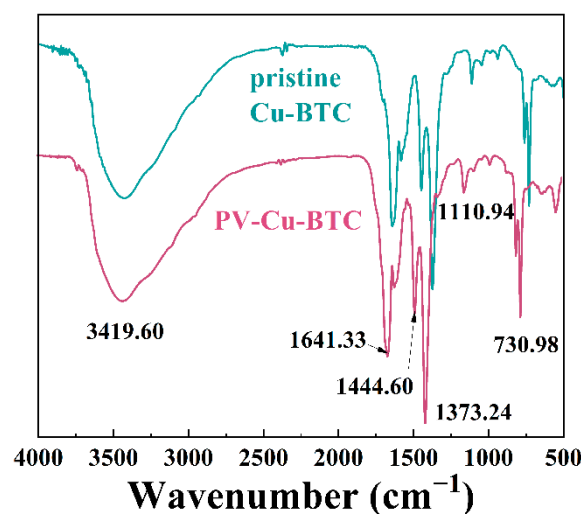


Figure 3. FT-IR spectra of pristine Cu-BTC and PV-Cu-BTC.

The specific surface area largely determined by the particle size of Cu-BTC is one of the most important key factors for pollutant adsorption performance. To this end, we measured the N_2 adsorption-desorption isotherms of prepared Cu-BTC with and without PVP modulation. As illustrated in Figure 4a, type-IV N_2 adsorption-desorption isotherms containing H3 loops are clearly found, suggesting the mesoporous structure of both PV-Cu-BTC and pristine Cu-BTC. Moreover, it can be also observed that N_2 uptake increases rapidly when the relative pressure is lower than 0.1. The maximum N_2 uptake for PV-Cu-BTC is much greater than that of pristine Cu-BTC. This observation highlights the larger specific surface area of PV-Cu-BTC over its counterpart. To quantitatively compare their microstructure diversities, the pore texture parameters of pristine Cu-BTC and PV-Cu-BTC were calculated, as shown in Table 2. After the modulation of PVP, the specific surface area of Cu-BTC could be increased to $1093.8 \text{ m}^2 \text{ g}^{-1}$, which is ca. 2.6 times that of the pristine one ($424.6 \text{ m}^2 \text{ g}^{-1}$). The average pore size is reduced from 2.71 to 2.38 nm while similar pore size distribution is recognized in Figure 4b. In particular, PV-Cu-BTC possesses a larger pore volume as compared to the pristine Cu-BTC. This result manifests that PV-Cu-BTC may have more adsorption sites than Cu-BTC for enhancing the pollutant removal capacity.

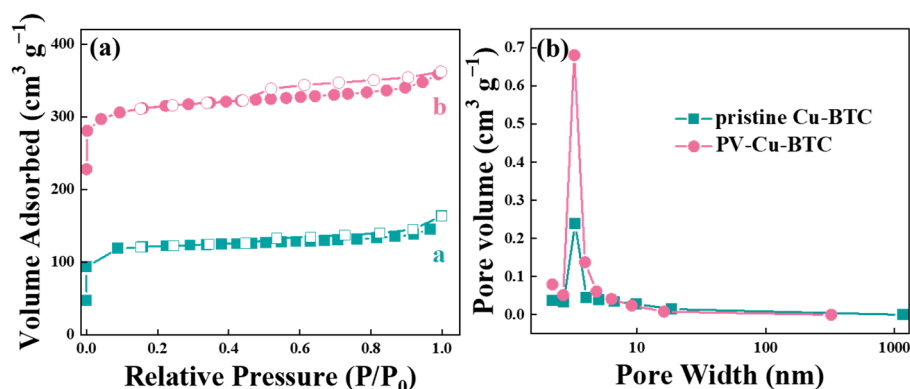


Figure 4. (a) N_2 adsorption-desorption isotherms and (b) pore size distribution curve of pristine Cu-BTC and PV-Cu-BTC.

Although PV-Cu-BTC exhibits a typical octahedral morphology of Cu-BTC, indicating successful formation of Cu-BTC, it is also necessary to determine the crystal structure of PV-Cu-BTC by using XRD technique. The XRD patterns of pristine Cu-BTC and PV-Cu-BTC are shown in Figure 5a. It is observed that both PV-Cu-BTC and pristine Cu-BTC samples appear to have similar characteristics in their diffraction peaks of the XRD patterns as the

previous report, in which the peaks at the 2θ of 6.6° , 9.4° , 11.52° , 13.34° , 18.96° , and 25.9° are assigned to (200), (220), (222), (400), (440), and (731) facets, respectively. Moreover, the diffraction peaks detected in these two XRD patterns are sharp and the corresponding half peak width is quite narrow. This indicates that a high crystallinity of PV-Cu-BTC is remained after the introduction of PVP modulator. The results show that PVP has no effect on the crystal structure of Cu-BTC so that the relevant crystal-dependent applications would be well preserved.

Table 2. Texture structure parameters of pristine Cu-BTC and PV-Cu-BTC.

Sample	S_{BET} ($\text{m}^2 \text{g}^{-1}$)	Average Pore Size (nm)
pristine Cu-BTC	424.597	2.713
PV-Cu-BTC	1093.764	2.381

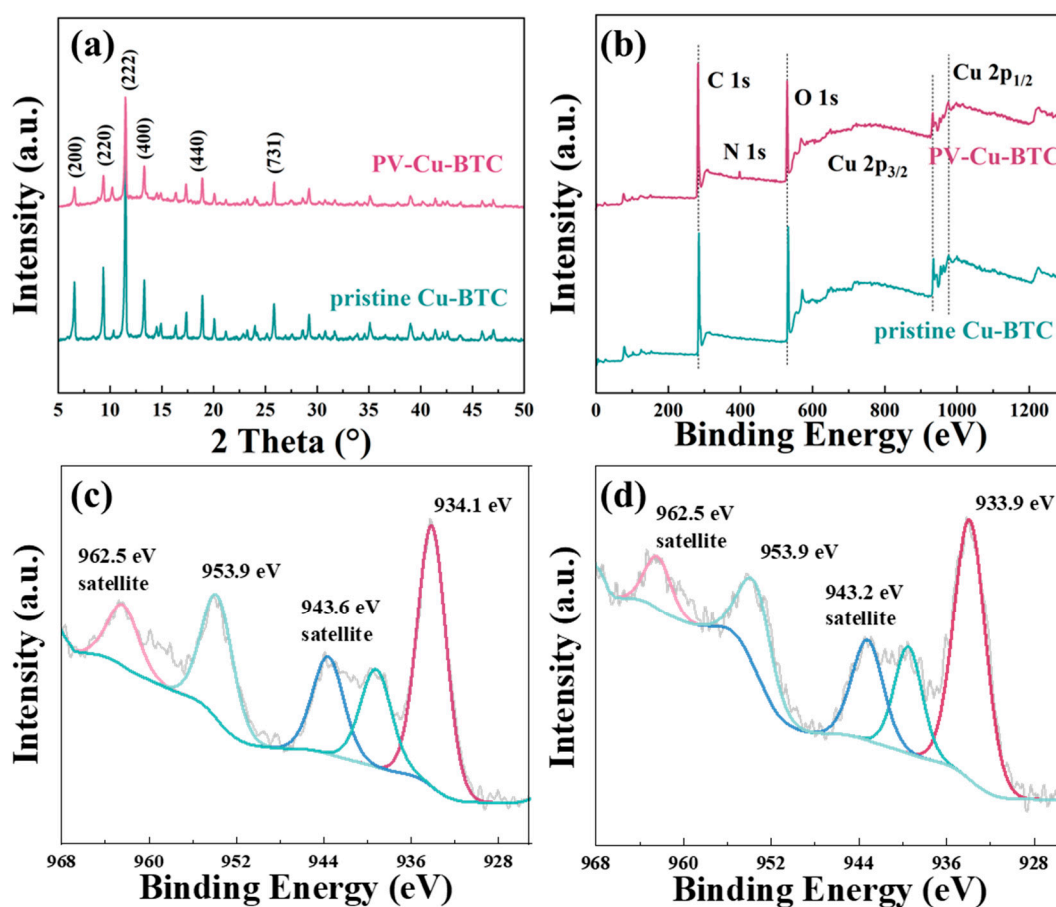


Figure 5. XRD patterns of Cu-BTC (a), survey XPS (b), Cu 2p XPS of pristine Cu-BTC (c) and Cu 2p XPS of PV-Cu-BTC (d).

To further elucidate the elemental composition and electronic structures of pristine Cu-BTC and PV-Cu-BTC, the XPS spectra were collected and analyzed. As shown in Figure 5b, it can be clearly observed that there are four main peaks located at 285.1, 532.1, 934.1, and 954.1 eV in the XPS survey spectra of pristine Cu-BTC and PV-Cu-BTC, corresponding to C 1s, O 1s, Cu 2p_{3/2}, and Cu 2p_{1/2}, respectively [35]. In particular, the newly generated peak at 399.1 eV could be attributed to the nitrogen element, which suggests the presence of trace PVP and in turns verifies the modulation function of PVP on the particle size of Cu-TBC. Figure 5c,d display the high-resolution Cu 2p XPS spectra of Cu-BTC with and without PVP modulation. The Cu 2p XPS spectra of as-synthesized catalysts are depicted around the range from 925 to 969 eV. The peaks locating at binding energies of 934.1 and

953.9 eV are assigned to Cu 2p_{3/2} and Cu 2p_{1/2}, respectively. Meanwhile, the well-known “shake-up satellite bands” (at the 936–947 and 961–965 eV regions) are clearly observed, which is indicative of the paramagnetic chemical state of Cu(II) [36]. However, in the case of PV-Cu-BTC, the bind energy of Cu 2p_{3/2} shifts from 934.1 to 933.9 eV and the intensity of shake-up satellite bands is also decreased slightly. These results indicate that the interaction of Cu(II) centers and N elements in PVP

3.3. Enhanced Adsorption Performance of PV-Cu-BTC

As previous reports have demonstrated that the adsorption performance is highly related to particle size and the specific surface area of MOFs, we first evaluated and compared the MB adsorption capacity of Cu-BTC with and without PVP modulation. As illustrated in Figure 6a, the maximum MB adsorption capacity of PVP-Cu-BTC is ca. 147.6 mg L^{−1} while the pristine Cu-BTC could only uptake 96.7 mg L^{−1} of MB adsorbent. This observation is well in agreement with the results of previous studies [37], greatly supporting the idea of enhancing the adsorption performance by particle size reduction.

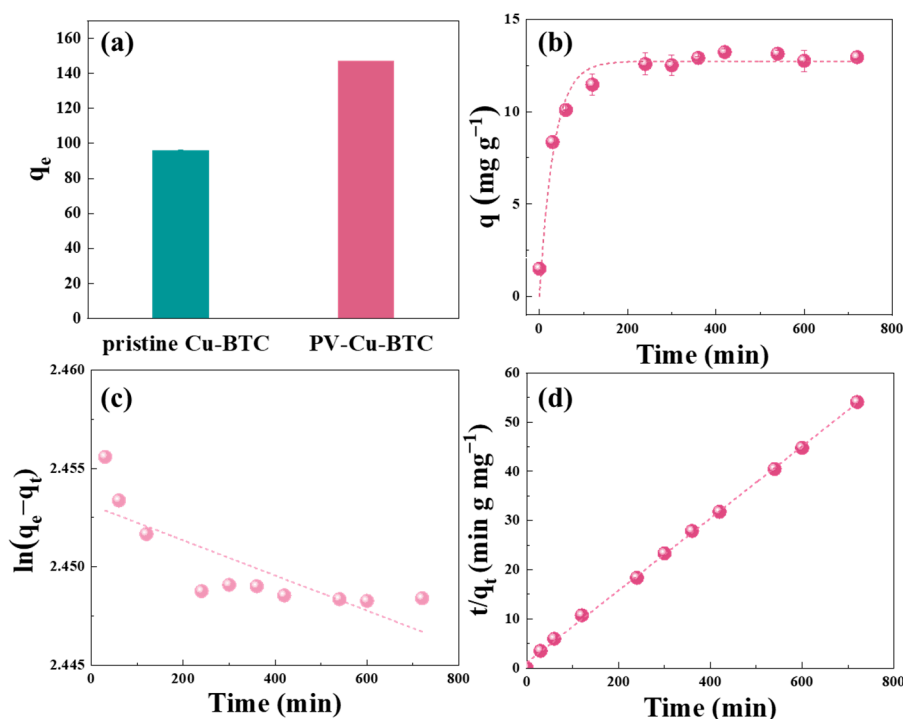


Figure 6. (a) MB adsorption capacity of pristine Cu-BTC and PV-Cu-BTC ($C_0 = 500$ mg L^{−1}, $m = 20$ mg, $V = 20$ mL, pH = 8, $T = 298$ K, and $t = 4$ h); (b) Effect of contact time on the adsorption of MB with PV-Cu-BTC ($C_0 = 20$ mg L^{−1}, $m = 150$ mg, $V = 150$ mL, pH = 8, $T = 298$ K, and $t = 12$ h); (c) pseudo-first-order and (d) pseudo-second-order model fitting curves of MB adsorption onto PV-Cu-BTC.

To further understand the enhanced adsorption performance, adsorption kinetics and isotherms of MB onto PV-Cu-BTC were investigated and elucidated. The effect of contact time on the MB adsorption capacity of PV-Cu-BTC is depicted in Figure 6b. On the one hand, the adsorbed amount of MB rapidly increased to a steady point at the first 60 min. On the other hand, the MB adsorption process was subjected to a balance at 240 min, when the equilibrium adsorption capacity of MB reached to 13.1 mg g^{−1}. In the first stage of adsorption, the electrostatic effect might be attributed to the rapid adsorption of MB by overcoming the diffusion resistance. In the second stage, as more sorption sites were invaded and steric hindrance increased, the more sorption rate was delayed [38,39]. The experimental adsorption data were fitted using the pseudo-first-order model and pseudo-

second-order model to investigate the kinetics insights of MB adsorption on the PV-Cu-BTC according to Equations (3) and (4):

$$\ln(q_e - q_t) = \ln q_e - k_1 t \quad (3)$$

$$\frac{t}{q_t} = \frac{1}{q_e^2 k_2} + \frac{1}{q_e} t \quad (4)$$

where k_1 (min^{-1}) and k_2 ($\text{g mg}^{-1} \text{min}^{-1}$) are the kinetic adsorption rate constants of the pseudo-first and second-order models, respectively; q_e (mg g^{-1}) and q_t (mg g^{-1}) are the adsorption capacity of MB onto PV-Cu-BTC at the equilibrium given interval time t (min), respectively. The kinetic parameters and correlation coefficients (R^2) for each model are summarized in Table 3. The relatively lower R^2 value in the case of fitting by pseudo-first-order model and the significant difference between the calculated and experimental adsorption capacity suggested that the pseudo-first-order model (Figure 6c) failed to describe well the MB adsorption process onto PV-Cu-BTC. Whereas, due to the higher R^2 value (0.9991) in the case of fitting by pseudo-second-order model and the similar adsorption capacity between experimental and fitting result, the MB adsorption process onto PV-Cu-BTC obeyed the pseudo-second-order model (Figure 6d). This indicates that chemisorption is a rate-limiting step in the MB adsorption by PV-Cu-BTC, which is consistent with previous results.

Table 3. Adsorption kinetic parameters for fitting results applying pseudo-first-order and pseudo-second-order models.

Adsorbent	Pseudo-First-Order Model			Pseudo-Second-Order Model		
	k_1 (min^{-1})	q_e (mg g^{-1})	R^2	k_2 ($\text{g mg}^{-1} \text{min}^{-1}$)	q_e (mg g^{-1})	R^2
PV-Cu-BTC	8.9209	12.7	0.6247	0.0733	13.1	0.9991

Since adsorption isotherms are considered a useful tool to describe the relationship between the adsorbate and adsorbent, the Langmuir and Freundlich isotherm models were applied to demonstrate the MB adsorption process according to Equations (5) and (6):

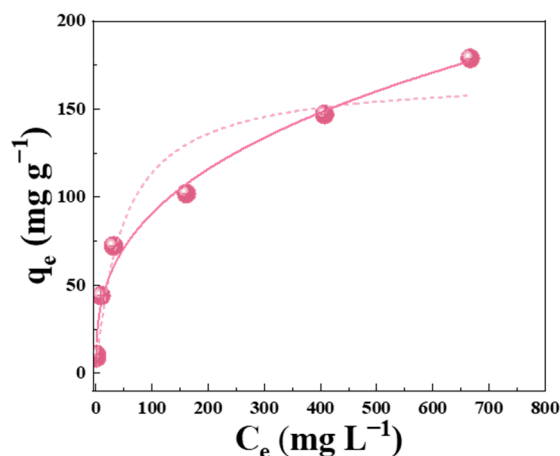
$$q_e = \frac{K_l q_m C_e}{1 + K_l C_e} \quad (5)$$

$$q_e = K_f C_e^f \quad (6)$$

where K_l (L mg^{-1}), q_m (mg g^{-1}), K_f ($\text{mg}^{1-f} \text{L}^f \text{g}^{-1}$) and f indicate the Langmuir adsorption constant, the maximum theoretical adsorption capacity, the Freundlich equilibrium constant and exponent, respectively. The isotherm parameters and correlation coefficients (R^2) for each model are summarized in Table 4. As shown in Figure 7, the adsorbed amount reaches a plateau at a higher equilibrium solution concentration. The highest adsorption capacity for MB arrives at 169.2 mg g^{-1} . Based on the fitting result, all the R^2 values from the Freundlich models of MB were much greater than those of the Langmuir isotherm models. This indicates that the Freundlich isotherm model is found to have a greater ability to fit the experimental data than the Langmuir isotherm model, demonstrating a multilayer adsorption of MB on the surface of PV-Cu-BTC [21,40]. In addition, the fitting result shows that the adsorption of MB on PV-Cu-BTC was greatly driven by both physical and chemical processes. The relatively larger specific surface area of PV-Cu-BTC could provide more accessible active adsorption sites for MB molecule captures in water. Once the active adsorption sites are fully occupied, the adsorption capacity of MB reaches the equilibrium stage with a saturation amount [41]. More importantly, the effect of other MOFs on MB removal was compared through literature data, as shown in Table 5. These results demonstrate that PV-Cu-BTC could be a promising adsorbent for removing dye from wastewater.

Table 4. Obtained key parameters from fitting results using pseudo-first-order and pseudo-second-order models.

Temperature (K)	Langmuir			<i>f</i>	Freundlich	
	K_L (L mg ^{−1})	q_m (mg g ^{−1})	R^2		K_f (g mg ^{−1} min ^{−1})	R^2
298	0.0206	169.2	0.9228	0.3522	17.9535	0.9832

**Figure 7.** MB Adsorption isotherms fitted by Langmuir model (dashed line) and Freundlich model (solid line).**Table 5.** Comparison of adsorption performance of PV-Cu-BTC toward MB removal over other reported MOFs counterparts.

Adsorbents	Adsorption Capacity (mg g ^{−1})	Reference
[BMIM][PF6]/MIL-53	204.9	[42]
MOF-235	187	[43]
MIL-101 MOFs	21	[44]
Ni-MOFs	156	[45]
HKUST-1/GO/Fe ₃ O ₄	105.9	[46]
Cu-BTC MOF	101.2	[47]
Fe ₃ O ₄ @ZIF-67	20	[48]
Fe ₃ O ₄ /HKUST-1	104	[49]
NiCu-BTC	798	[50]
VNU-23	1992	[51]
Zn-MOF	326	[52]
PV-Cu-BTC	169.2	This Work

3.4. Adsorption Stability of PV-Cu-BTC

As various pH values are a typical feature in different wastewater resources, it is necessary to investigate the effect of pH value on the adsorption stability reflecting the practicality of adsorbent. It can be clearly observed in Figure 8a that the adsorption rate and removal efficiency of MB by PV-Cu-BTC almost remained unchanged at different pH values ranging from 4.0 to 10.0. To elucidate this observation, the zeta potentials of PV-Cu-BTC at different pH values were determined and shown in Figure 8a. It was found that PV-Cu-BTC exhibited a negative surface charge over the wide pH range (4.0–10.0), which allowed the negative PV-Cu-BTC to adsorb cation MB molecules via electrostatic attraction. Besides, π - π interaction would also participate in the adsorption process due to the presence of a benzene ring in both the PV-Cu-BTC and MB molecular structures. As for extreme alkali condition (e.g., pH 11.0), the adsorption efficiency for MB suffered a slight decline probably because the three-dimensional pore structure of PV-Cu-BTC might be destroyed at this condition [53].

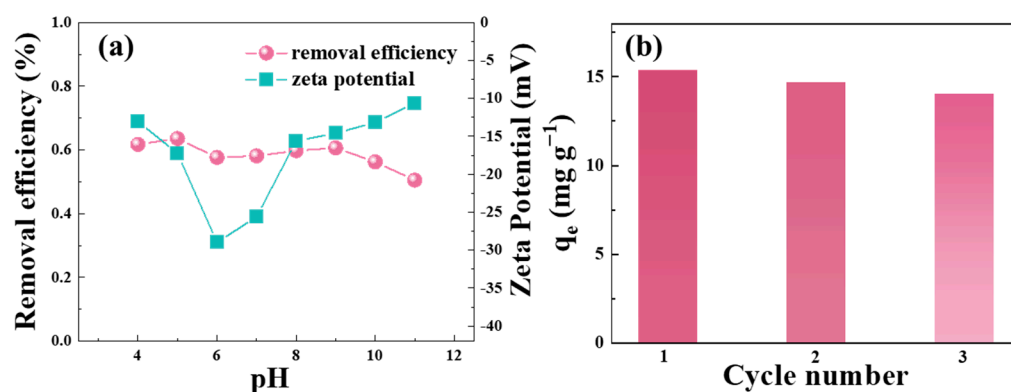


Figure 8. (a) Effect of pH value on MB adsorption onto PV-Cu-BTC; (b) PV-Cu-BTC on MB during regeneration cycles ($C_0 = 20 \text{ mg L}^{-1}$, $m = 25 \text{ mg}$, $V = 25 \text{ mL}$, $\text{Ph} = 8$, $T = 298 \text{ K}$, and $t = 4 \text{ h}$).

3.5. Desorption and Regeneration of PV-Cu-BTC

To evaluate the possibility of regeneration and reusability of PV-Cu-BTC as an adsorbent, the desorption experiments were performed. Desorption and regeneration experiments were performed using ethanol. The results of MB adsorption for three cycles are shown in Figure 8b. It can be clearly observed that more than 60% of MB can be removed after 3 cycles. The results show that PV-Cu-BTC has good recycling performance and could be a potential water purification material.

3.6. Possible Adsorption Mechanism

According to the previous discussion, we propose a possible mechanism for the adsorption of MB on PV-Cu-BTC (Figure 9). First, the regulation of PVP increased the specific surface area of Cu-BTC, which favored the overall adsorption process. Since $-\text{OH}$ and $\text{C}=\text{O}$ on PV-Cu-BTC were electronegative, they would bind to positively charged MB through electrostatic attraction and hydrogen bond. In addition, the BTC ligands of PV-Cu-BTC possessed a benzene ring that also showed affinity to MB molecules via π - π interaction. These driving forces may be responsible for the enhanced adsorption of PV-Cu-BTC, however, much effort should be made to understand the involved specific mechanism.

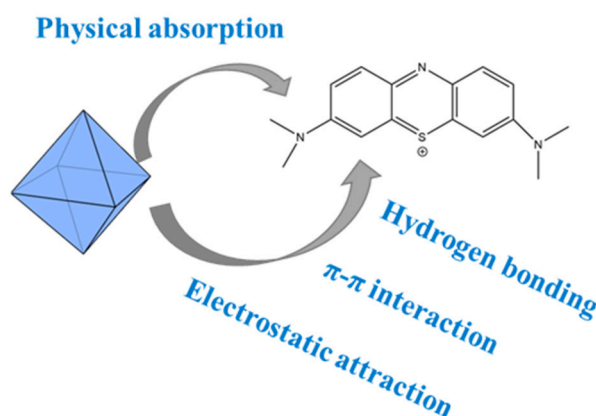


Figure 9. Possible adsorption mechanism of PV-Cu-BTC.

4. Conclusions

In summary, we demonstrated a practical and facile approach to regulate the particle size of Cu-BTC adsorbents with high tunability by screening the functional modulator of various surfactants adding in hydrothermal synthesis procedure. These surfactants showed a very different modulation capacity in reducing Cu-BTC's particle size, in which PVP outperformed the other five surfactants in the effective modulation of Cu-BTC's particle size.

By slightly increasing PVP concentration to 0.14 mmol L^{-1} , the average particle size of Cu-BTC could be correspondingly reduced by more than ten times, reaching to a comparative smaller value of $2.4 \mu\text{m}$ than reported counterparts. The resulting PV-Cu-BTC retained the crystalline structure of pristine Cu-BTC while the specific surface area was largely increased for the enhancement of MB adsorption. Pseudo-second-order and Freundlich isotherm models were found to well describe the adsorption processes of MB by PV-Cu-BTC. The theoretical maximum adsorption capacity reached up to 169.2 mg g^{-1} , which is much higher than those of emerging analogues reported so far. This work may provide a practical strategy to engineer MOFs' particle size for enhanced adsorption application.

Author Contributions: Conceptualization, S.W., T.Y., M.W. and D.Y.; methodology, M.Z. and Q.H.; software, S.W.; validation, M.Z.; formal analysis, L.Z. and K.T.; investigation, S.W., L.X., K.T. and D.Y.; resources, M.W.; data curation, L.Z., L.X. and Q.H.; writing—original draft preparation, S.W.; writing—review and editing, T.Y. and D.Y.; Visualization; supervision, and project administration, M.W.; funding acquisition, D.Y. All authors have read and agreed to the published version of the manuscript.

Funding: This research was funded by the National Natural Science Foundation of China (grant number 22106141), the Funding of Zhejiang Sci-Tech University (grant number LW-YP2021032) and the Postdoctoral Program (grant number TYY202103) of Zhejiang Sci-Tech University Tongxiang Research Institute.

Institutional Review Board Statement: Not applicable.

Informed Consent Statement: Not applicable.

Data Availability Statement: Not applicable.

Conflicts of Interest: The authors declare no conflict of interest.

References

- Li, L.; Liu, X.L.; Geng, H.Y.; Hu, B.; Song, G.W.; Xu, Z.S. A MOF/graphite oxide hybrid (MOF: HKUST-1) material for the adsorption of methylene blue from aqueous solution. *J. Mater. Chem. A* **2013**, *1*, 10292–10299. [\[CrossRef\]](#)
- Luo, J.M.; Fu, K.X.; Yu, D.Y.; Hristovski, K.D.; Westerhoff, P.; Crittenden, J.C. Review of Advances in Engineering Nanomaterial Adsorbents for Metal Removal and Recovery from Water: Synthesis and Microstructure Impacts. *ACS EST Eng.* **2021**, *1*, 623–661. [\[CrossRef\]](#)
- Johari, N.A.; Yusof, N.; Lau, W.J.; Abdullah, N.; Salleh, W.N.W.; Jaafar, J.; Aziz, F.; Ismail, A.F. Polyethersulfone ultrafiltration membrane incorporated with ferric-based metal-organic framework for textile wastewater treatment. *Sep. Purif. Technol.* **2021**, *270*, 118819. [\[CrossRef\]](#)
- Pazdzior, K.; Bilinska, L.; Ledakowicz, S. A review of the existing and emerging technologies in the combination of AOPs and biological processes in industrial textile wastewater treatment. *Chem. Eng. J.* **2019**, *376*, 120597. [\[CrossRef\]](#)
- Zhang, J.; Zhou, Z.; Feng, Z.; Zhao, H.; Zhao, G. Fast Generation of Hydroxyl Radicals by Rerouting the Electron Transfer Pathway via Constructed Chemical Channels during the Photo-Electro-Reduction of Oxygen. *Environ. Sci. Technol.* **2022**, *56*, 1331–1340. [\[CrossRef\]](#)
- Nidheesh, P.V.; Zhou, M.; Oturan, M.A. An overview on the removal of synthetic dyes from water by electrochemical advanced oxidation processes. *Chemosphere* **2018**, *197*, 210–227. [\[CrossRef\]](#) [\[PubMed\]](#)
- Pandey, S.; Son, N.; Kang, M. Synergistic sorption performance of karaya gum crosslink poly(acrylamide-co-acrylonitrile) @ metal nanoparticle for organic pollutants. *Int. J. Biol. Macromol.* **2022**, *210*, 300–314. [\[CrossRef\]](#) [\[PubMed\]](#)
- Khapse, M.; Shekhawat, A.; Saravanan, D.; Pandey, S.; Jugade, R. Mesoporous Fe–Al-doped cellulose for the efficient removal of reactive dyes. *Mater. Adv.* **2022**, *3*, 3278–3285. [\[CrossRef\]](#)
- Gupta, R.; Pandit, C.; Pandit, S.; Gupta, P.K.; Lahiri, D.; Agarwal, D.; Pandey, S. Potential and future prospects of biochar-based materials and their applications in removal of organic contaminants from industrial wastewater. *J. Mater. Cycles Waste Manag.* **2022**, *24*, 852–876. [\[CrossRef\]](#)
- Huang, T.; Yan, M.; He, K.; Huang, Z.; Zeng, G.; Chen, A.; Peng, M.; Li, H.; Yuan, L.; Chen, G. Efficient removal of methylene blue from aqueous solutions using magnetic graphene oxide modified zeolite. *J. Colloid Interface Sci.* **2019**, *543*, 43–51. [\[CrossRef\]](#)
- Lu, H.; Zhang, L.; Wang, B.; Long, Y.; Zhang, M.; Ma, J.; Khan, A.; Chowdhury, S.P.; Zhou, X.; Ni, Y. Cellulose-supported magnetic Fe₃O₄-MOF composites for enhanced dye removal application. *Cellulose* **2019**, *26*, 4909–4920. [\[CrossRef\]](#)
- Luo, J.; Maier, R.M.; Yu, D.; Liu, B.; Zhu, N.; Amy, G.L.; Crittenden, J.C. Double-Network Hydrogel: A Potential Practical Adsorbent for Critical Metals Extraction and Recovery from Water. *Environ. Sci. Technol.* **2022**, *56*, 4715–4717. [\[CrossRef\]](#) [\[PubMed\]](#)

13. Wu, G.G.; Ma, J.P.; Li, S.; Guan, J.; Jiang, B.; Wang, L.Y.; Li, J.H.; Wang, X.Y.; Chen, L.X. Magnetic copper-based metal organic framework as an effective and recyclable adsorbent for removal of two fluoroquinolone antibiotics from aqueous solutions. *J. Colloid Interface Sci.* **2018**, *528*, 360–371. [\[CrossRef\]](#)
14. Han, P.P.; Xia, Y. Thiol-functionalized metal-organic framework for highly efficient removal of bromate from water. *J. Environ. Chem. Eng.* **2018**, *6*, 3384–3391. [\[CrossRef\]](#)
15. DeCoste, J.B.; Peterson, G.W.; Schindler, B.J.; Killops, K.L.; Browe, M.A.; Mahle, J.J. The effect of water adsorption on the structure of the carboxylate containing metal-organic frameworks Cu-BTC, Mg-MOF-74, and UiO-66. *J. Mater. Chem. A* **2013**, *1*, 11922–11932. [\[CrossRef\]](#)
16. Ke, F.; Qiu, L.G.; Yuan, Y.P.; Peng, F.M.; Jiang, X.; Xie, A.J.; Shen, Y.H.; Zhu, J.F. Thiol-functionalization of metal-organic framework by a facile coordination-based postsynthetic strategy and enhanced removal of Hg²⁺ from water. *J. Hazard. Mater.* **2011**, *196*, 36–43. [\[CrossRef\]](#)
17. Yang, Y.; Shukla, P.; Wang, S.; Rudolph, V.; Chen, X.-M.; Zhu, Z. Significant improvement of surface area and CO₂ adsorption of Cu-BTC via solvent exchange activation. *RSC Adv.* **2013**, *3*, 17065–17072. [\[CrossRef\]](#)
18. Hamon, L.; Jolimaite, E.; Pirmgruber, G.D. CO₂ and CH₄ Separation by Adsorption Using Cu-BTC Metal-Organic Framework. *Ind. Eng. Chem. Res.* **2010**, *49*, 7497–7503. [\[CrossRef\]](#)
19. Bordiga, S.; Regli, L.; Bonino, F.; Groppo, E.; Lamberti, C.; Xiao, B.; Wheatley, P.S.; Morris, R.E.; Zecchina, A. Adsorption properties of HKUST-1 toward hydrogen and other small molecules monitored by IR. *Phys. Chem. Chem. Phys.* **2007**, *9*, 2676–2685. [\[CrossRef\]](#) [\[PubMed\]](#)
20. Chiericatti, C.; Carlos Basilico, J.; Zapata Basilico, M.L.; Manuel Zamaro, J. Novel application of HKUST-1 metal-organic framework as antifungal: Biological tests and physicochemical characterizations. *Microporous Mesoporous Mater.* **2012**, *162*, 60–63. [\[CrossRef\]](#)
21. Abbasi, A.R.; Karimi, M.; Daasbjerg, K. Efficient removal of crystal violet and methylene blue from wastewater by ultrasound nanoparticles Cu-MOF in comparison with mechanosynthesis method. *Ultrason. Sonochem.* **2017**, *37*, 182–191. [\[CrossRef\]](#)
22. Gong, X.; Zhao, R.; Qin, J.; Wang, H.; Wang, D. Ultra-efficient removal of NO in a MOFs-NTP synergistic process at ambient temperature. *Chem. Eng. J.* **2019**, *358*, 291–298. [\[CrossRef\]](#)
23. Wee, L.H.; Lohe, M.R.; Janssens, N.; Kaskel, S.; Martens, J.A. Fine tuning of the metal-organic framework Cu-3(BTC)(2) HKUST-1 crystal size in the 100 nm to 5 micron range. *J. Mater. Chem.* **2012**, *22*, 13742–13746. [\[CrossRef\]](#)
24. Van Assche, T.R.C.; Desmet, G.; Ameloot, R.; De Vos, D.E.; Terryn, H.; Denayer, J.F.M. Electrochemical synthesis of thin HKUST-1 layers on copper mesh. *Microporous Mesoporous Mater.* **2012**, *158*, 209–213. [\[CrossRef\]](#)
25. Zou, F.; Yu, R.; Li, R.; Li, W. Microwave-assisted synthesis of HKUST-1 and functionalized HKUST-1-@H3PW12O40: Selective adsorption of heavy metal ions in water analyzed with synchrotron radiation. *Chemphyschem* **2013**, *14*, 2825–2832. [\[CrossRef\]](#)
26. Al-Janabi, N.; Hill, P.; Torrente-Murciano, L.; Garforth, A.; Gorgojo, P.; Siperstein, F.; Fan, X. Mapping the Cu-BTC metal-organic framework (HKUST-1) stability envelope in the presence of water vapour for CO₂ adsorption from flue gases. *Chem. Eng. J.* **2015**, *281*, 669–677. [\[CrossRef\]](#)
27. Osborn Popp, T.M.; Plantz, A.Z.; Yaghi, O.M.; Reimer, J.A. Precise Control of Molecular Self-Diffusion in Isorecticular and Multivariate Metal-Organic Frameworks. *Chemphyschem* **2020**, *21*, 32–35. [\[CrossRef\]](#)
28. Senkovska, I.; Kaskel, S. Ultrahigh porosity in mesoporous MOFs: Promises and limitations. *Chem. Commun.* **2014**, *50*, 7089–7098. [\[CrossRef\]](#)
29. Zhang, W.-p.; Zou, C.-d.; Zhao, B.-g.; Zhai, Q.-j.; Gao, Y.-l. Size control and its mechanism of SnAg nanoparticles. *Trans. Nonferrous Met. Soc. China* **2014**, *24*, 750–757. [\[CrossRef\]](#)
30. Chen, Y.; Zhang, J.; Zhang, M.; Wang, X. Molecular and textural engineering of conjugated carbon nitride catalysts for selective oxidation of alcohols with visible light. *Chem. Sci.* **2013**, *4*, 3244–3248. [\[CrossRef\]](#)
31. Seoane, B.; Castellanos, S.; Dikhtiarenko, A.; Kapteijn, F.; Gascon, J. Multi-scale crystal engineering of metal organic frameworks. *Coord. Chem. Rev.* **2016**, *307*, 147–187. [\[CrossRef\]](#)
32. Pan, Y.; Heryadi, D.; Zhou, F.; Zhao, L.; Lestari, G.; Su, H.; Lai, Z. Tuning the crystal morphology and size of zeolitic imidazolate framework-8 in aqueous solution by surfactants. *CrystEngComm* **2011**, *13*, 6937–6940. [\[CrossRef\]](#)
33. Loera-Serna, S.; Oliver-Tolentino, M.A.; de Lourdes López-Núñez, M.; Santana-Cruz, A.; Guzmán-Vargas, A.; Cabrera-Sierra, R.; Beltrán, H.I.; Flores, J. Electrochemical behavior of [Cu₃(BTC)₂] metal-organic framework: The effect of the method of synthesis. *J. Alloys Compd.* **2012**, *540*, 113–120. [\[CrossRef\]](#)
34. Hartmann, M.; Kunz, S.; Himsl, D.; Tangermann, O.; Ernst, S.; Wagener, A. Adsorptive separation of isobutene and isobutane on Cu₃(BTC)₂. *Langmuir* **2008**, *24*, 8634–8642. [\[CrossRef\]](#)
35. Wi-Afedzi, T.; Kwon, E.; Tuan, D.D.; Lin, K.-Y.A.; Ghanbari, F. Copper hexacyanoferrate nanocrystal as a highly efficient non-noble metal catalyst for reduction of 4-nitrophenol in water. *Sci. Total Environ.* **2020**, *703*, 134781. [\[CrossRef\]](#)
36. Luo, Q.-x.; An, B.-w.; Ji, M.; Park, S.-E.; Hao, C.; Li, Y.-q. Metal-organic frameworks HKUST-1 as porous matrix for encapsulation of basic ionic liquid catalyst: Effect of chemical behaviour of ionic liquid in solvent. *J. Porous Mater.* **2014**, *22*, 247–259. [\[CrossRef\]](#)
37. Eren, M.Ş.A.; Arslanoğlu, H.; Çiftçi, H. Production of microporous Cu-doped BTC (Cu-BTC) metal-organic framework composite materials, superior adsorbents for the removal of methylene blue (Basic Blue 9). *J. Environ. Chem. Eng.* **2020**, *8*, 104247. [\[CrossRef\]](#)
38. Ho, Y.-S. Review of second-order models for adsorption systems. *J. Hazard. Mater.* **2006**, *136*, 681–689. [\[CrossRef\]](#)

39. Yu, D.; Wang, Y.; Wu, M.; Zhang, L.; Wang, L.; Ni, H. Surface functionalization of cellulose with hyperbranched polyamide for efficient adsorption of organic dyes and heavy metals. *J. Clean. Prod.* **2019**, *232*, 774–783. [\[CrossRef\]](#)
40. Sabouni, R.; Aidan, A.; AlObeidli, A.; Lahib, F.; Bacha, H.H.; Kassermally, R.; Jarmakani, S. Adsorption kinetics and thermodynamics of Methylene Blue by HKUST-1. *Desalination Water Treat.* **2019**, *138*, 301–312. [\[CrossRef\]](#)
41. Luo, J.M.; Yu, D.Y.; Hristovski, K.D.; Fu, K.X.; Shen, Y.W.; Westerhoff, P.; Crittenden, J.C. Critical Review of Advances in Engineering Nanomaterial Adsorbents for Metal Removal and Recovery from Water: Mechanism Identification and Engineering Design. *Environ. Sci. Technol.* **2021**, *55*, 4287–4304. [\[CrossRef\]](#)
42. Kavak, S.; Durak, O.; Kulak, H.; Polat, H.M.; Keskin, S.; Uzun, A. Enhanced Water Purification Performance of Ionic Liquid Impregnated Metal-Organic Framework: Dye Removal by BMIM PF₆ /MIL-53(Al) Composite. *Front. Chem.* **2021**, *8*, 1277. [\[CrossRef\]](#)
43. Haque, E.; Jun, J.W.; Jhung, S.H. Adsorptive removal of methyl orange and methylene blue from aqueous solution with a metal-organic framework material, iron terephthalate (MOF-235). *J. Hazard. Mater.* **2011**, *185*, 507–511. [\[CrossRef\]](#)
44. Huang, X.-X.; Qiu, L.-G.; Zhang, W.; Yuan, Y.-P.; Jiang, X.; Xie, A.-J.; Shen, Y.-H.; Zhu, J.-F. Hierarchically mesostructured MIL-101 metal-organic frameworks: Supramolecular template-directed synthesis and accelerated adsorption kinetics for dye removal. *CrystEngComm* **2012**, *14*, 1613–1617. [\[CrossRef\]](#)
45. Zhao, S.Q.; Chen, D.; Wei, F.H.; Chen, N.N.; Liang, Z.; Luo, Y. Synthesis of graphene oxide/metal-organic frameworks hybrid materials for enhanced removal of Methylene blue in acidic and alkaline solutions. *J. Chem. Technol. Biotechnol.* **2018**, *93*, 698–709. [\[CrossRef\]](#)
46. Li, L.; Liu, X.L.; Gao, M.; Hong, W.; Liu, G.Z.; Fan, L.; Hu, B.; Xia, Q.H.; Liu, L.; Song, G.W.; et al. The adsorption on magnetic hybrid Fe₃O₄/HKUST-1/GO of methylene blue from water solution. *J. Mater. Chem. A* **2014**, *2*, 1795–1801. [\[CrossRef\]](#)
47. Kaur, R.; Kaur, A.; Umar, A.; Anderson, W.A.; Kansal, S.K. Metal organic framework (MOF) porous octahedral nanocrystals of Cu-BTC: Synthesis, properties and enhanced adsorption properties. *Mater. Res. Bull.* **2019**, *109*, 124–133. [\[CrossRef\]](#)
48. Yang, Q.; Ren, S.; Zhao, Q.; Lu, R.; Hang, C.; Chen, Z.; Zheng, H. Selective separation of methyl orange from water using magnetic ZIF-67 composites. *Chem. Eng. J.* **2018**, *333*, 49–57. [\[CrossRef\]](#)
49. Wang, R.; Ge, C.; Tianzhu, X.; Yuanyuan, Z.; Zhang, Y.; Zhang, X. Facile synthesis of magnetic hybrid metal organic frameworks with high adsorption capacity for methylene blue. *Appl. Organomet. Chem.* **2017**, *31*, e3798. [\[CrossRef\]](#)
50. Abd El Salam, H.M.; Zaki, T. Removal of hazardous cationic organic dyes from water using nickel-based metal-organic frameworks. *Inorg. Chim. Acta* **2018**, *471*, 203–210. [\[CrossRef\]](#)
51. Bui, T.T.M.; Nguyen, L.T.; Pham, N.P.H.; Tran, C.C.; Nguyen, L.T.; Nguyen, T.A.; Nguyen, H.N.; Nguyen, M.V. A new approach for ultra-high adsorption of cationic methylene blue in a Zr-sulfonic-based metal-organic framework. *RSC Adv.* **2021**, *11*, 36626–36635. [\[CrossRef\]](#)
52. Zhang, J.; Li, F.; Sun, Q. Rapid and selective adsorption of cationic dyes by a unique metal-organic framework with decorated pore surface. *Appl. Surf. Sci.* **2018**, *440*, 1219–1226. [\[CrossRef\]](#)
53. Zhuang, J.-L.; Ceglarek, D.; Pethuraj, S.; Terfort, A. Rapid Room-Temperature Synthesis of Metal Organic Framework HKUST 1 Crystals in Bulk and as Oriented and Patterned Thin Films. *Adv. Funct. Mater.* **2011**, *21*, 1442–1447. [\[CrossRef\]](#)